Physics of Plasmas

Instability of nonlinear Trivelpiece-Gould waves. II. Weakly trapped particles

Cite as: Phys. Plasmas **26**, 102113 (2019); https://doi.org/10.1063/1.5116376
Submitted: 24 June 2019 . Accepted: 19 September 2019 . Published Online: 16 October 2019

Daniel H. E. Dubin

COLLECTIONS

EP This paper was selected as an Editor's Pick

ARTICLES YOU MAY BE INTERESTED IN

Instability of nonlinear Trivelpiece-Gould waves I: Wave degeneracies
Physics of Plasmas **26**, 102111 (2019); https://doi.org/10.1063/1.5116375

Criterion for the sign of wave energy
Physics of Plasmas **26**, 102106 (2019); https://doi.org/10.1063/1.5120401

Quantum hydrodynamics for plasmas–Quo vadis?
Physics of Plasmas **26**, 090601 (2019); https://doi.org/10.1063/1.5097885

AIP Publishing

Physics of Plasmas ARTICLE scitation.org/journal/php

Instability of nonlinear Trivelpiece-Gould waves. II. Weakly trapped particles

Cite as: Phys. Plasmas **26**, 102113 (2019); doi: 10.1063/1.5116376
Submitted: 24 June 2019 · Accepted: 19 September 2019 ·
Published Online: 16 October 2019

Daniel H. E. Dubin

AFFILIATIONS

Department of Physics, UCSD, La Jolla, California 92093, USA

ABSTRACT

This paper discusses a novel parametric instability mechanism caused by particles that are weakly trapped in the potential wells of a nonlinear "pump" wave. The pump wave is unstable to the growth of daughter waves with longer wavelength and nearly the same phase velocity as the pump. This induces adjacent potential peaks in the wave to slowly approach one-another, receding from other pairs of peaks. Particles that are weakly trapped between approaching peaks, with kinetic energies just below the potential maxima, are heated by compression and escape the well, and then become retrapped on the other side of the approaching peaks, where they amplify the compression by pushing the peaks together. The mechanism applies to low-collisionality plasmas supporting waves with near-acoustic dispersion relations such as ion sound waves, magnetized Langmuir waves, or Alfvén waves. The theory is compared to particle in cell simulations of Trivelpiece-Gould (TG) traveling waves, as well as to experiments on pure ion plasmas that observe parametric instability in TG standing waves.

I. INTRODUCTION

In this paper, we discuss a newly discovered parametric decay instability mechanism[1] that involves kinetic effects caused by a distribution of particles trapped in the potential wells of a nonlinear pump wave. The mechanism causes exponential growth of daughter waves that deplete the pump, with similar features to those observed in recent experiments.[2] The mechanism differs from well-known kinetic processes such as nonlinear Landau damping/growth,[3] which involves a nonlinear wave-particle resonance, or the sideband instability,[4,5] which involves a wave resonance with trapped particles. Here, no wave-particle resonance condition needs to be met. This allows instability to develop over a broad range of daughter wavenumbers and frequencies, causing strong wave damping and plasma heating in the nonlinear stage.

The linear theory of the instability is described here for waves with nearly acoustic dispersion relations (such as Alfvén or ion–acoustic waves), but the mechanism could contribute to wave instability even if this is not the case. It should therefore be applicable to a range of nonlinear plasma waves that involve trapped particles. Here, we apply the theory to nonlinear electrostatic Trivelpiece-Gould (TG) waves[6,7] propagating along a plasma column.

In the kinetic decay instability discussed here, peaks in the wave potential and density move with respect to one-another. Some peaks move closer together, and others recede from their neighbors. This motion is replicated along the wavetrain, creating a periodic structure. (This structure is the growing daughter wave or waves.) Particles trapped between approaching wave peaks are heated by compression, while particles trapped between peaks receding from one-another are cooled. This heating and cooling of the trapped particles would normally produce restoring pressure forces that push back against the motion of the peaks.

However, particles that are "weakly trapped," i.e., with energies close to the wave potential maxima, can gain enough energy in the compressional heating so as to become untrapped. These untrapped particles are then immediately retrapped as they reflect from, and lose energy to, a receding potential peak, and are then cooled between the adjacent receding peaks. These weakly trapped particles have "switched sides" and now help push the peaks further together. This detrapping and retrapping of weakly trapped particles can change the sign of the pressure force, causing it to amplify the motion of the peaks. In effect, the weakly trapped particles have negative compressibility, which destabilizes the nonlinear wave.

Other instabilities have also been identified that rely on or involve trapped particles, such as the previously mentioned sideband instability, as well as a negative mass instability that causes trapped particles to bunch.[8] In addition, other authors have noted the strong effects that trapped particles can have on the effective compressibility associated with nonlinear plasma waves.[9] Perhaps the most important difference with this previous work is the focus here on weakly trapped particles that are exchanged between different trapping potential wells.

If the motion of the potential peaks is slow compared to the bounce time of the weakly trapped particles, one can treat the heating, detrapping, retrapping, and cooling using adiabatic theory, which simplifies the analysis. This adiabatic limit is a good approximation for a nearly acoustic dispersion relation, where the phase velocity of the growing daughter waves is nearly the same as that of the pump wave.

In Sec. II, we consider a simple model of the instability that captures the basic mechanism. This "moving wall" model was first introduced in Ref. 1 for daughter waves with twice the pump wavelength, and is extended here to describe the instability for daughter waves with arbitrary wavelength. We find that all wavelengths are unstable, but the maximum growth rate occurs for daughter waves with twice the pump wavelength.

In Sec. III, we briefly review the fluid theory of nonlinear TG traveling waves, and discuss linear perturbations to the waves. We focus on low-frequency perturbations, since these are most easily driven unstable by the negative compressibility of weakly trapped particles. We show that for large amplitude pump waves these low-frequency eigenmodes correspond to the translational motions of the potential peaks mentioned above.

In Sec. IV, we develop a kinetic theory of particles weakly trapped in the pump wave potential and derive general expressions for the growth rate of the resulting instability. We also consider a simpler version of the general theory that applies to large amplitude sharply peaked pump waves, eventually recovering the results of the moving wall model as a limit.

In Sec. V, we compare these theory expressions to particle-in-cell simulations of nonlinear TG waves, finding close agreement between the measured growth rates in the simulations and the theoretical predictions of the general theory. The results are also in fair agreement with the simpler theory models in their applicable large amplitude regimes.

In Sec. VI, we compare experimental results on the instability observed in TG standing waves to full r-z particle simulations in realistic geometry of the experiments. Growth rates in these simulations have similar behavior compared to the experimental measurements with regard to the amplitude dependence of the growth rate as well as to the temperature dependence. Also, by removing trapped particles from the simulations, we find that we can turn off the instability.

In Sec. VII, we briefly discuss the results and consider some open questions.

II. MOVING WALL MODEL

A simple moving wall model for this instability mechanism elucidates the rather counterintuitive "negative-compressibility" behavior of weakly trapped particles under adiabatic compressions and expansions.[1] Consider the maximum growth-rate case for which adjacent potential peaks, initially evenly spaced by 2π, move in opposite directions. When two such peaks, say n and $n-1$, move toward one-another by a distance $\delta L(t)$, the trapped distribution between them is adiabatically compressed, and the next two peaks (n and $n+1$) recede from one-another by the same distance, causing particles trapped between them to be adiabatically expanded (see Fig. 1). The velocity distribution for the compressed particles changes from $f_{T0}(v)$ to

$$f_1(v) = f_{T0}(v(1-\lambda)), \tag{1}$$

where $\lambda = \delta L/(2\pi)$ is the fractional change in the distance between adjacent peaks. The change in density of the compressed trapped particles is then

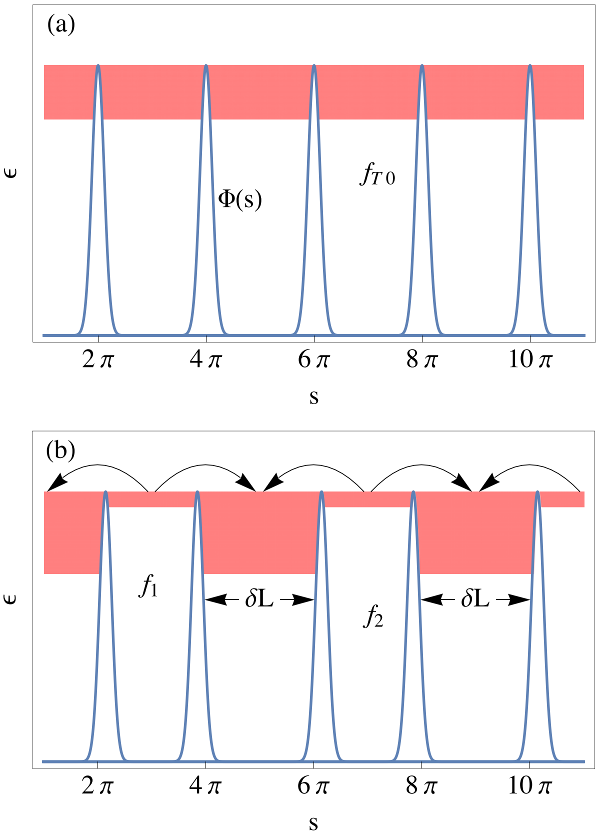

FIG. 1. (a) Initial potential $\Phi(s)$ for a large amplitude wave, and the band of occupied energies $\epsilon = v^2/2 + \Phi(s)$ in a distribution f_{T0} of weakly trapped particles. Untrapped particles are not displayed as they play no role in the instability. (b) Potential and particle energies after the peaks shift positions as the instability grows. Weakly trapped particles are detrapped and retrapped as they undergo adiabatic compression and expansion.

$$\begin{aligned}\delta n_1 &= 2\int_0^{v_{max}} dv(f_1(v) - f_{T0}(v)) \\ &= -2\lambda \int_0^{v_{max}} dv(f_{T0}(v_{max}) - f_{T0}(v)),\end{aligned} \tag{2}$$

where $v_{max} = \sqrt{2\Phi_{max}}$ is the maximum speed of a trapped particle (assumed to have unit mass) and Φ_{max} is the potential maximum. In the second line, we Taylor-expanded to first order in λ, and performed an integration by parts. For a weakly trapped distribution with $f_{T0}(v_{max}) > f_{T0}(v)$ in the integrand of Eq. (2), the density change on compression is *negative*. This is because, on compression, weakly trapped particles are heated until they become untrapped, lowering the trapped particle density in the compressed well. These detrapped particles do not, however, join the untrapped particle distribution. They are instead immediately retrapped in an expanding potential well as they lose energy on reflection from one of the receding peaks, see Fig. 1. Images and an animation of the detrapping and retrapping, taken from particle simulations of the process, can be found in Ref. 1 as well as in Sec. V of this paper.

For particles trapped in an expanding potential well, the distribution changes from $f_{T0}(v)$ to $f_2(v)$ where

$$f_2(v)=\begin{cases} f_{T0}(v(1+\lambda)), & 0<v<v_{max}/(1+\lambda),\\ f_{T0}(2v_{max}-v(1+\lambda)), & \dfrac{v_{max}}{1+\lambda}<v<v_{max}. \end{cases} \tag{3}$$

The second form of $f_2(v)$ comes from particles that were lost from a compressed well and retrapped in the expanding well. Integrating Eq. (3) over velocity one finds that the change in density δn_2 for particles in this expanding well is $\delta n_2=-\delta n_1$, which also follows directly from particle conservation. In the expanding potential well, density increases for a weakly trapped distribution because of the addition to the well of particles retrapped from the compressed well.

To analyze instability of the pump wave in this process, we consider the change in energy of the trapped particles in the two adjacent potential wells during the motion of the potential peaks along the chain. The total kinetic energy change δK of these trapped particles is

$$\begin{aligned}\delta K(t)&=4\pi\int_0^{v_{max}}dv\frac{v^2}{2}[(1-\lambda)f_1+(1+\lambda)f_2-2f_{T0}]\\ &=-\beta\delta L(t)^2,\end{aligned}\tag{4}$$

where in the second line we performed a Taylor expansion to second order in λ using Eqs. (1) and (3), and where the expansion coefficient β is found to be given by

$$\beta=\frac{6}{2\pi}\int_0^{v_{max}}dv v^2(f_{T0}(v_{max})-f_{T0}(v)).\tag{5}$$

The energy change is second order in δL because reflection symmetry requires δK to be independent of the sign of δL. For a weakly trapped particle distribution, $\beta>0$ and this kinetic energy change is negative, implying that the trapped particles give up energy that can drive instability. The coefficient β can be thought of as a coefficient of negative compressibility for these trapped particles.

The total fluid energy associated with motion of the two adjacent peaks (which move by $\delta L/2$ and $-\delta L/2$ respectively) is $\delta E=\mathcal{M}(\delta\dot{L}/2)^2+\mathcal{K}\delta L^2$. The first term is the kinetic energy of the two peaks, each with inertial mass $\mathcal{M}$ associated with their translation, and the second is potential energy associated with a nearest-neighbor repulsive interaction of the peaks with those on either side (the wave peaks of a TG wave are concentrations of like-sign charge, screened from one-another by the surrounding electrode structure). A method of determining the "spring constant" $\mathcal{K}$ and the inertial mass $\mathcal{M}$ will be described later. By conservation of energy $\delta E+\delta K=0$, which implies the overall energy budget for the system has the harmonic oscillator form

$$\frac{\mathcal{M}}{4}\left(\frac{d\delta L}{dt}\right)^2+(\mathcal{K}-\beta)\delta L^2=0.\tag{6}$$

Thus, the kinetic energy $\delta K=-\beta\delta L^2$ of the weakly trapped particles acts as a negative potential energy contribution to the overall energy, thanks to the adiabatic approximation whereby the trapped particle kinetic energy is a reversible function of the configuration of the wave system.

The differential equation (6) for δL has exponentially growing and decaying solutions with growth rate,

$$\Gamma=\sqrt{\frac{4(\beta-\mathcal{K})}{\mathcal{M}}}.\tag{7}$$

Instability occurs provided $\beta>\mathcal{K}$, so that the destabilizing negative compressibility β of weakly trapped particles overcomes the repulsive spring constant κ between pump wave density peaks, changing the sign of the potential energy term in Eq. (6).

This moving wall model can be easily modified to allow for general motions of the potential peaks, for a particular choice of trapped particle distribution function. As before we take peaks initially at equally spaced positions $s_n=2\pi n$, n an integer. Between each peak there are trapped particles, and for simplicity, we assume that their distribution is a uniform phase space density f_{T0} for $v_{min}<v<v_{max}$, and is zero for lower speeds, as shown in Fig. 1(a). We allow each peak to slowly vary from its initial position by a small amount δs_n. As the potential wells between peaks compress or expand and particles are traded between wells through adiabatic detrapping and retrapping, the phase-space density of trapped particles remains at the uniform equilibrium value f_{T0}, but over a new range of speeds $v_n<v<v_{max}$ [see Fig. 1(b)], where $v_n=v_{min}/(1+\lambda_n)$, and where $\lambda_n=(\delta s_n-\delta s_{n-1})/(2\pi)$ is the fractional change in displacement between adjacent potential peaks.

Now, consider the force δF_n on peak n due to trapped particles with speed v. This force is the momentum change per unit time caused by trapped particle reflections from the peak. To evaluate this, the momentum change per reflection, $2v$, is multiplied by the phase-space particle flux $f_{T0}v$, and integrated over v, accounting for particles reflecting from both sides of the peak

$$\begin{aligned}\delta F_n&=\int_{v_n}^{v_{max}}dvf_{T0}2v^2-\int_{v_{n+1}}^{v_{max}}dvf_{T0}2v^2\\ &=2f_{T0}v_{min}^3(\lambda_n-\lambda_{n+1})\\ &=-2f_{T0}v_{min}^3\frac{\delta s_{n+1}-2\delta s_n+\delta s_{n-1}}{2\pi},\end{aligned}\tag{8}$$

where the second line uses a Taylor expansion assuming small changes in the peak position. To this force, we add the force due to repulsion between adjacent peaks, $\delta F_{Rn}=-\mathcal{K}(\delta s_n-\delta s_{n-1}-\delta s_{n+1}+\delta s_n)$.

We use this force to evaluate the acceleration of the nth peak via $\mathcal{M}\delta\ddot{s}_n=\delta F_n+\delta F_{Rn}$. A dispersion relation can then be obtained by assuming that $\delta s_n\propto\exp(i\mu s_n-i\omega t)$ for some wavevector μ. When used in Newton's law, this yields

$$\omega^2=4\frac{\mathcal{K}-\beta}{\mathcal{M}}\sin^2(\mu\pi),\tag{9}$$

where $\beta=f_{T0}v_{min}^3/\pi$, as expected from Eq. (5). This exhibits instability for all wavenumbers $\mu\neq0$ whenever $\beta>\mathcal{K}$, with maximum growth when $\mu=1/2$. This wavenumber corresponds to adjacent peaks in the pump wave moving in opposite directions, the case considered in the discussion surrounding Eq. (7).

III. FLUID THEORY OF TG PUMP WAVES

In this section, we review some relevant characteristics of the fluid theory of TG waves, which will be required for the general kinetic theory of the trapped particle instability. TG waves are compressional electrostatic traveling waves in a magnetically confined cylindrical plasma column.[10,11] Cylindrically symmetric TG waves that are without radial nodes can be approximately described by coupled evolution equations for the plasma density $N(z,t)$, the fluid velocity $V(z,t)$, and the plasma potential $\Phi(z,t)$, where z is the axial position and t is time.[6,12] These fluid functions have been averaged radially over the plasma column to remove radial dependence and simplify the theory. For a cold plasma, neglecting thermal effects and the trapped particles, the evolution equations are the continuity, momentum, and Poisson equations for the cold fluid

$$\frac{\partial N}{\partial t} + \frac{\partial}{\partial z}(\mathrm{V}N) = 0, \tag{10}$$

$$\frac{\partial \mathrm{V}}{\partial t} + \frac{\partial}{\partial z}\left(\frac{1}{2}\mathrm{V}^2 + \Phi\right) = 0, \tag{11}$$

$$\frac{\partial^2 \Phi}{\partial z^2} - k_\perp^2 \Phi = -N + 1, \tag{12}$$

where the perpendicular wavenumber $k_\perp$ is determined by the plasma radius and radius of the surrounding cylindrical electrode structure. Here, and throughout the paper, we employ dimensionless variables, with density scaled by the equilibrium density n_0, times scaled by the equilibrium plasma frequency $\omega_p = \sqrt{4\pi q^2 n_0/m}$, and distances scaled by the wavenumber k_f of the pump wave. The scaled potential energy Φ is in units of $m\omega_p^2/k_f^2$.

As discussed in Refs. 1, 6, and 7, it is useful to work in the frame of the traveling wave, and define the fluid velocity $V \equiv \mathrm{V} - u$ with respect to this wave frame, where u is the wave speed as seen from the lab frame. In the wave frame, Eqs. (10)–(12) can be written as

$$\frac{\partial N}{\partial t} + \frac{\partial}{\partial s}(VN) = 0, \tag{13}$$

$$\frac{\partial V}{\partial t} + \frac{\partial}{\partial s}\left(\frac{1}{2}V^2 + \Phi\right) = 0, \tag{14}$$

$$\frac{\partial^2 \Phi}{\partial s^2} - k_\perp^2 \Phi = -N + 1, \tag{15}$$

where $s \equiv z - ut$ is position measured in the wave frame. In this frame, the traveling wave is stationary, with $N = N_0(s)$, $V = V_0(s)$, and $\Phi = \Phi_0(s)$ where N_0, V_0, and Φ_0 are solutions to the time-independent versions of Eqs. (13)–(15)

$$\frac{\partial}{\partial s}(V_0 N_0) = 0, \tag{16}$$

$$\frac{\partial}{\partial s}\left(\frac{1}{2}V_0{}^2 + \Phi_0\right) = 0, \tag{17}$$

$$\frac{\partial^2 \Phi_0}{\partial s^2} - k_\perp^2 \Phi_0 = -N_0 + 1. \tag{18}$$

These solutions are parametrized by the amplitude A of the wave, defined here and in Refs. 1, 6, and 7 as the amplitude of the first Fourier harmonic of the density,

$$A \equiv \int_0^{2\pi} \frac{ds}{2\pi} N_0(s) \exp(-is). \tag{19}$$

The origin of the coordinate s is chosen at a maximum of the wave, so that N_0, V_0, and Φ_0 are even functions of s; and so A is real (and positive-definite).

The wave speed u is a monotonically increasing function of the pump wave amplitude A, and also depends on $k_\perp$, and is given by Eq. (68) in Ref. 6. For small A, the wave is nearly a single Fourier mode with wave speed $u = u_1 + 0(A^2)$ where

$$u_k \equiv 1/\sqrt{k^2 + k_\perp^2} \tag{20}$$

is the linear phase speed of TG waves with wavenumber k (measured in our dimensionless units). The density and velocity are, respectively, $N_0(s) = 1 + 2A\cos(s) + 0(A^2)$, $V_0(s) = -u_1 + 2Au_1\cos(s) + 0(A^2)$. This may be verified by substitution of these solutions into Eqs. (13)–(15), keeping terms only up to first order in A. Higher order terms in an expansion in small A for each of these quantities, and numerical solutions for larger A values, can be found in Ref. 6.

As A or $k_\perp$ increases, it was found that the pump wave peaks become higher and sharper, while the troughs become broader (see Fig. 2, Fig. 5 in Ref. 6, or Fig. 1 in Ref. 7). This general behavior is common to many nonlinear wave systems, including k-dV, Boussinesq, and Stokes waves. The steady solutions are a balance between dispersion (controlled by $k_\perp$), which tends to broaden the wave peaks, and nonlinearity, which tends to steepen the peaks. Smaller dispersion (i.e., larger $k_\perp$) or larger amplitude A therefore causes more steepening of the wave profile. When $k_\perp$ and A are both large, the wavetrain can be characterized roughly as a chain of weakly interacting solitons; i.e., a uniformly spaced sequence of sharp, well-separated, individual peaks.

A. Fluid stability of TG pump waves

The stability of small fluid perturbations to these steady pump wave solutions has also been investigated, both analytically and numerically.[6,7] In the wave frame, the perturbations satisfy the linearized fluid equations,

$$\frac{\partial \delta N}{\partial t} + \frac{\partial}{\partial s}(V_0 \delta N + N_0 \delta V) = 0, \tag{21}$$

$$\frac{\partial \delta V}{\partial t} + \frac{\partial}{\partial s}(V_0 \delta V + \delta\Phi) = 0, \tag{22}$$

$$\frac{\partial^2 \delta\Phi}{\partial s^2} - k_\perp^2 \delta\Phi = -\delta N. \tag{23}$$

We consider solutions of these equations using periodic boundary conditions with period $2\pi M$, M a positive integer. Because the pump wave is a time-independent flow in the pump wave frame, the perturbations to the pump wave take the form of a linear superposition of normal modes. Each mode has perturbed density $\delta N(s, t)$, fluid

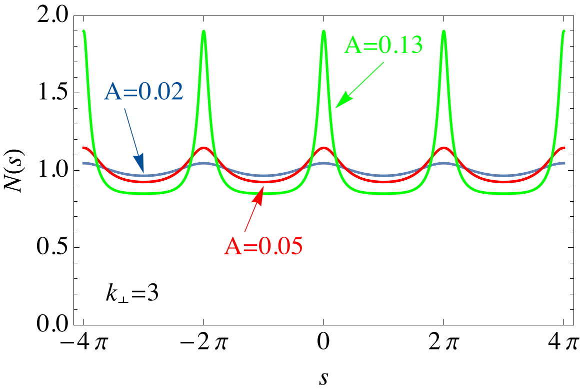

FIG. 2. TG pump waves for perpendicular wavenumber $k_\perp = 3$, at three amplitudes A.

velocity $\delta V(s,t)$, and potential $\delta\Phi(s,t)$. The time dependence of these normal modes is of the form $\exp(-i\omega_0 t)$ where ω_0 is a (possibly complex) mode frequency. Furthermore, since the pump wave is periodic in s, Floquet theory implies that each normal mode is doubly periodic in position with s dependence of the form $\exp(i\mu s)f(s)$, where f is some periodic function with the pump wave period 2π, and μ is any wavenumber that matches the boundary conditions, in the range $-1/2 < \mu \leq 1/2$ [adding an integer to μ merely redefines $f(s)$].[7] For periodicity $2\pi M$, this implies that μ takes the values $\mu = n/M$ for integers n in the range $[-M/2, M/2]$. For a given value of μ in this range, there is a countably infinite set of normal modes.

More progress can be made by writing the coupled mode equations (21)–(23) in vector form,[1]

$$i\omega_0\psi(s) = \hat{L}\cdot\psi(s) \equiv \frac{\partial}{\partial s}\begin{pmatrix} V_0(s) & N_0(s) \\ \hat{G} & V_0(s) \end{pmatrix}\cdot\psi(s)$$

$$= \frac{\partial}{\partial s}\begin{pmatrix} V_0\delta N + N_0\delta V \\ \delta\Phi + V_0\delta V \end{pmatrix}, \qquad (24)$$

where $\psi = (\delta N, \delta V)$ is a vector normal mode, $\hat{L}$ is the above-defined matrix integrodifferential operator, and $\hat{G}$ is the Green's function operator for the linearized Poisson equation (23), defined by $\hat{G}\delta N = \delta\Phi$. These vector normal modes can be shown to form an orthogonal set with respect to a generalized matrix inner product defined by its action on any two vector functions $\psi_1(s)$ and $\psi_2(s)$

$$[\psi_1, \psi_2] \equiv \frac{1}{4}\int \frac{ds}{2\pi M}\,\psi_1^*(s)\cdot\begin{pmatrix} \hat{G}^\dagger & V_0(s) \\ V_0(s) & N_0(s) \end{pmatrix}\cdot\psi_2(s), \qquad (25)$$

where $\hat{G}^\dagger$ is the left Green's function operator, defined by $\delta N\hat{G}^\dagger = \delta\Phi$, and the integral over s runs over a displacement of $2\pi M$.

The inner product of an eigenmode with itself is the energy δE (per unit length) of that eigenmode

$$[\psi,\psi] = \delta E = \frac{1}{4}\int \frac{ds}{2\pi M}\{N_0(s)|\delta V(s)|^2$$

$$+2V_0(s)Re[\delta N(s)^*\delta V(s)] + \delta\Phi(s)^*\delta N(s)\}. \qquad (26)$$

Also, the matrix operator $\hat{L}$ can be shown to be anti-Hermitian with respect to this inner product

$$[\psi_1, \hat{L}\psi_2] = -[\hat{L}\psi_1, \psi_2], \qquad (27)$$

and this leads to several results; in particular, a proof that ω_0 is real provided that $\delta E \neq 0$, and that the eigenmodes form an orthogonal set.

The frequency spectrum of these normal modes was examined using analytical methods valid for small pump amplitude, and numerical methods based on Hill's method[13] for larger amplitudes.[7] Modes were shown to come in complex-conjugate pairs: for every mode with frequency ω_0 and given perturbed density and velocity, there is a corresponding mode with frequency $-\omega_0^*$, and complex conjugate perturbed density and velocity (which implies that it has a μ value of opposite sign).

For low pump amplitudes, the eigenmodes have spatial form close to $\exp(iks)$ for given wavenumber k and frequencies close to the frequency of linear TG modes as seen in the frame of the pump wave. There are two branches corresponding to the two directions of propagation

$$\omega_0^{\pm}(k) = -ku_1 \pm ku_k, \quad A \ll 1. \qquad (28)$$

Using the numerical frequency spectra as well as analytical theory, it was shown that for narrow ranges of the wavenumber k (depending on $k_\perp$ and A) there are frequency degeneracies between pairs of eigenmodes that cause the pump wave to become weakly unstable to the growth of the degenerate modes.[7] The superposition of degenerate modes forms a perturbation with energy $\delta E = 0$, allowing ω_0 to be complex. However, it was found that the derived instability growth rates are too small to explain observed growth in current experiments.[2]

1. Fluid theory of low frequency perturbations to large amplitude pump waves

Here, we will further examine the low frequency fluid eigemodes on a pump wave of large amplitude, since it will turn out that these low-frequency eigenmodes are the most easily driven unstable by the presence of trapped particles in the pump waves.

In Fig. 3, we compare Eq. (28) to the numerically determined frequencies from Hill's method, focussing on the low-frequency regime. The frequencies are plotted vs wavenumber μ for the three pump wave amplitudes shown in Fig. 2. For low amplitude, the frequencies are close to $\omega_0^+(k)$ (the solid curves in the plot, plotted vs $\mu = k - n$ where the integer n is chosen so that the result for μ falls in the range $[-1/2, 1/2]$).

At large amplitude, the low-frequency eigenmodes have frequencies that are well-matched by the functional form $\omega_0 = \pm\alpha\sin\pi\mu$, with α a decreasing function of both pump amplitude A and $k_\perp$. One might recognize this type of dispersion relation from condensed-matter physics: It is the dispersion relation obtained for a one-dimensional chain of identical masses connected by springs. The low-frequency eigenmodes of the pump wave obey this type of dispersion relation because at large amplitudes the pump wave resembles a chain

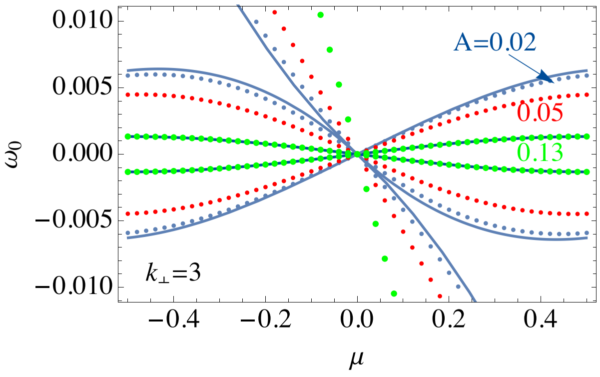

FIG. 3. Eigenmode frequencies vs wavenumber μ for the three pump waves shown in Fig. 2 (dots), focusing on low frequency modes. For the small amplitude case $A = 0.02$ these are close to the low-amplitude theory $\omega_0^+(k)$ (solid curves). For the large ampliude case $A = 0.13$ a fit to the data of the form $\pm\alpha\sin(\pi k)$ works well (curves through the data, with $\alpha = 1.33\times10^{-3}$).

of weakly interacting solitons: a set of narrow well-separated peaks (see Fig. 2) with density, potential, and velocity well-approximated by

$$\begin{aligned} N_0(s) &= N_0(\pi) + \sum_n N_s(s-2\pi n), \\ \Phi_0(s) &= \Phi_0(\pi) + \sum_n \Phi_s(s-2\pi n), \\ V_0(s) &= V_0(\pi) + \sum_n V_s(s-2\pi n), \end{aligned} \tag{29}$$

where $\Phi_s(x)$, $V_s(x)$ and $N_s(x)$ are sharply peaked functions, symmetric in x, approaching zero for $|x| \to \pi$.

The lowest frequency eigenmodes on this pump wave are long wavelength perturbations that move the pump wave peaks with respect to one another without changing the shape of the peaks very much; for example, the potential in the mode can be approximately represented as

$$\Phi(s,t) = \Phi_0(\pi) + \sum_n \Phi_s(s - 2\pi n - \delta s_n(t)), \tag{30}$$

where $\delta s_n(t)$ is the change in position of the nth peak; and similarly for the density and velocity. So Taylor expanding to first order in δs_n, the perturbed density, potential, and velocity in the normal mode have the approximate form

$$\begin{aligned} \delta N &= -\sum_n \delta s_n(t) N_s'(s-2\pi n), \\ \delta \Phi &= -\sum_n \delta s_n(t) \Phi_s'(s-2\pi n), \\ \delta V &= -\sum_n \delta s_n(t) V_s'(s-2\pi n). \end{aligned} \tag{31}$$

An example of such a mode is displayed in Fig. 4, for $\mu = 1/8$. As shown in the figure, the change in density is well-represented by the derivative of the pump wave peaks, with the amplitudes of each peak multiplied by

$$\delta s_n = \delta s_{max} \exp(i\mu s_n - i\omega_0 t), \quad s_n = 2\pi n, \tag{32}$$

where δs_{max} is the maximum displacement amplitude in the mode. This form for δs_n has a spatial dependence that is consistent with Floquet's theorem.

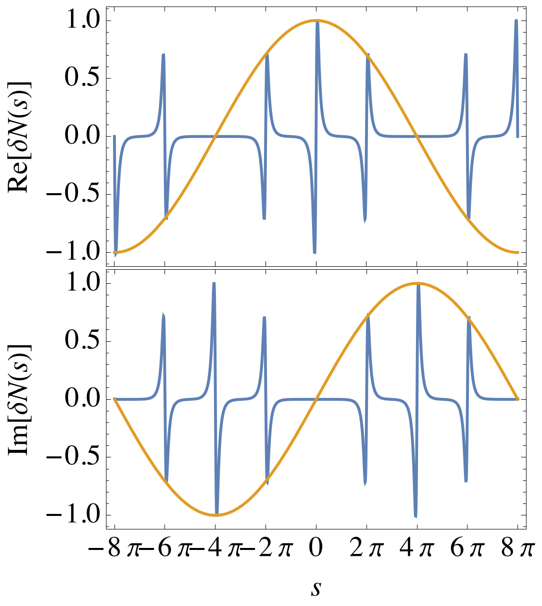

FIG. 4. Real and imaginary parts of the perturbed density in the lowest-frequency eigenmode for $k_\perp = 3, A = 0.13$, and $\mu = 1/8$, plotted over one wavelength of the mode. Overlayed on this mode are $\cos(\mu s)$ and $\sin(\mu s)$.

These types of modes are low frequency because there is little restoring force to the motion of peaks with respect to one-another; the near-solitons interact very weakly with one-another when they are far apart compared to their width. If we posit the potential interaction between peaks as nearest neighbor with a linear restoring force constant $\mathscr{K}$, we then obtain a spectrum given by the longitudinal modes of wavenumber μ on a chain of identical particles of mass $\mathscr{M}$[14] with nearest-neighbor separation 2π,

$$\omega_0^2(\mu) = \frac{4\mathscr{K}}{\mathscr{M}} \sin^2(\pi\mu). \tag{33}$$

This simple model explains the observed frequency dependence on wavenumber for the low-frequency modes, with the ratio $\alpha^2 = 4\mathscr{K}/\mathscr{M}$ obtained from the fit to the frequency data.

The simple chain model also explains the energy of the low-frequency modes found from the Hills method and Eq. (26). This energy is plotted in Fig. 5 vs μ for the large amplitude case $A = 0.13$, $k_\perp = 3$. For a longitudinal normal mode with wavenumber μ on a chain of M particles (periodically replicated) with harmonic nearest-neighbor interactions, the total energy is $M\mathscr{M}\omega_0^2(\mu)\delta s_{max}^2/2$ and so the energy per unit length is

$$\delta E_0 = \frac{1}{4\pi} \mathscr{M} \omega_0^2(\mu) \delta s_{max}^2. \tag{34}$$

The numerically determined energy for these low-frequency modes is well-fit by Eq. (34), taking Eq. (33) for $\omega_0(\mu)$ (see Fig. 5). Now, the value of the mode normalization constant δs_{max} can be determined independently by fitting the eigenmodes to the functional forms given in Eq. (31), with $N_s'(s) = N_0'(s), -\pi < s < \pi$, and $N_s'(s) = 0$ otherwise; and similarly for V_s and Φ_s. With δs_{max} known from this fit, a fit of the energy to the form given in Eq. (34) determines the mass $\mathscr{M}$ associated with each peak in the pump wave. This

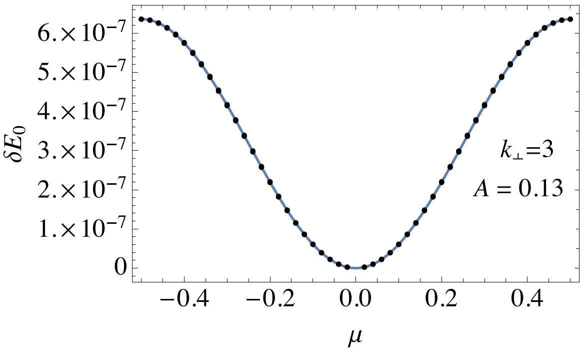

FIG. 5. Energy per unit length of the low-frequency modes vs wavenumber μ for the case of a pump wave with $A = 0.13$ and $k_\perp = 3$, determined from Hills method (dots) and from a fit to Eq. (34) (curve). Here, we obtain from the fit that $\mathscr{M} = 1.92$, having obtained δs_{max} from a separate fit described in the text.

method of determining the mass is more accurate than the approximation for the mass based on soliton energy that was used in Ref. 1. Once we know the mass and the mode frequency, we can also obtain the spring constant $\mathscr{K}$ via $\omega_0(\mu = 1/2) = 2\sqrt{\mathscr{K}/\mathscr{M}}$.

IV. KINETIC THEORY OF PUMP WAVE PARAMETRIC INSTABILITY

We will now consider the destabilization of the low-frequency eigenmodes to the pump wave caused by weakly trapped particles. We add a particle "tail" distribution $f_T(s, v, t)$ to the cold plasma, making an overall density of $N(s,t) + N_T(s,t)$ where $N_T = \int dv f_T$ is the density of tail particles. These tail particles model an energy spread to the cold plasma distribution. The tail distribution can include particles trapped in the pump wave potential wells. What follows is an expanded and clarified version of the theory described in Ref. 1.

The tail particles couple to the fluid density N through their effect on the plasma potential Φ. To determine this effect, we include the tail density $N_T(s,t)$ in Eq. (15)

$$\frac{\partial^2 \Phi}{\partial s^2} - k_\perp^2 \Phi = -N - N_T + 1. \tag{35}$$

The tail particles are assumed to satisfy the Vlasov equation,

$$\frac{\partial f_T}{\partial t} + v\frac{\partial f_T}{\partial s} - \frac{\partial \Phi}{\partial s}\frac{\partial f_T}{\partial v} = 0. \tag{36}$$

The tail particles change both the pump wave solution and the perturbations to the pump wave. In the stationary pump wave, the tail particles form a Bernstein-Greene-Kruskal (BGK) state[15] with a distribution function depending only on particle energy $\epsilon = v^2/2 + \Phi(s)$: $f_T = f_{T0}(\epsilon)$. The cold plasma density and fluid velocity are then shifted from $N_0(s)$ and $V_0(s)$ to $N(s)$ and $V(s)$, respectively, where these functions satisfy the time-independent versions of Eqs. (13) and (14),

$$\frac{\partial}{\partial s}(VN) = 0, \tag{37}$$

$$\frac{\partial}{\partial s}\left(\frac{1}{2}V^2 + \Phi\right) = 0, \tag{38}$$

along with Eq. (35).

Throughout we will assume that the tail particle density is small and work to first order in this density. In this case, we can write $N = N_0 + N_1$, $V = V_0 + V_1$, $\Phi = \Phi_0 + \Phi_1$ where N_1, V_1, Φ_1 are the small corrections to the fluid pump wave density, velocity, and potential caused by the tail particles. These corrections satisfy linearized versions of Eqs. (35), (37), and (38),

$$\frac{\partial}{\partial s}(V_0 N_1 + N_0 V_1) = 0, \tag{39}$$

$$\frac{\partial}{\partial s}(V_0 V_1 + \Phi_1 + \Phi_{T0}) = 0, \tag{40}$$

$$\frac{\partial^2 \Phi_1}{\partial s^2} - k_\perp^2 \Phi_1 = -N_1, \tag{41}$$

$$\frac{\partial^2 \Phi_{T0}}{\partial s^2} - k_\perp^2 \Phi_{T0} = -N_{T0}, \tag{42}$$

where $N_{T0}(s) = \int dv f_{T0}(\epsilon)$ is the equilibrium tail particle density in the stationary pump wave (as seen in the wave frame), and Φ_{T0} is the potential corresponding to this density.

Time-dependent small perturbations on this nonlinear pump wave satisfy

$$\frac{\partial \delta N}{\partial t} + \frac{\partial}{\partial s}(V\delta N + N\delta V) = 0, \tag{43}$$

$$\frac{\partial \delta V}{\partial t} + \frac{\partial}{\partial s}(V\delta V + \delta\Phi) = 0, \tag{44}$$

$$\frac{\partial^2 \delta\Phi}{\partial s^2} - k_\perp^2 \delta\Phi = -\delta N - \delta N_T, \tag{45}$$

where the perturbed tail particle density $\delta N_T = \int dv \delta f_T$, and the perturbed tail particle distribution δf_T satisfies the linearized Vlasov equation

$$\frac{\partial \delta f_T}{\partial t} + v\frac{\partial \delta f_T}{\partial s} - \frac{\partial \Phi}{\partial s}\frac{\partial \delta f_T}{\partial v} + \frac{\partial \delta\Phi}{\partial s}\frac{\partial f_{T0}}{\partial v} = 0. \tag{46}$$

We will simplify the Vlasov response of the tail particles by assuming that the evolution of perturbations to the pump wave is slow compared to the time scale associated with tail particle motion in the stationary pump wave, so that adiabatic theory is a good approximation. Then, Eq. (46) can be integrated to obtain[16]

$$\delta f_T = \frac{\partial f_{T0}}{\partial \epsilon}(\delta\Phi(s) - \langle\delta\Phi\rangle(\epsilon)), \tag{47}$$

where $\langle\delta\Phi\rangle(\epsilon)$ is the bounce-average of $\delta\Phi(s)$ around a particle orbit of energy ϵ

$$\langle\delta\Phi\rangle(\epsilon) = \frac{1}{\tau(\epsilon)}\oint \frac{ds}{v(\epsilon, s)}\delta\Phi(s), \tag{48}$$

$\tau(\epsilon) = \oint ds/v(\epsilon, s)$ is the period of the orbit, and $v(\epsilon, s)$ is the particle speed at energy ϵ, satisfying $v^2/2 + \Phi(s) = \epsilon$. The adiabatic approximation relies on the assumption that $\omega_0 \tau \ll 1$ where ω_0 is the frequency of the fluid motions. The main effect of this approximation is to neglect Landau resonances in the response of the tail particles to the pump wave perturbations.

We consider the effect of the tail particles on a fluid eigenmode $\psi = (\delta N, \delta V)$, keeping terms only to first order in the tail particle density. We separate out all terms involving the tail density in Eqs. (43)–(45), and use the matrix operator notation of Eq. (24), obtaining

$$i\omega\psi = \hat{L}\cdot\psi + \hat{C}\cdot\psi, \tag{49}$$

where ω is the frequency of the eigenmode, shifted from ω_0 by the tail particles, and the operator $\hat{C}$ involves the tail particle terms

$$\hat{C}\cdot\psi = \frac{\partial}{\partial s}\begin{pmatrix} V_1\delta N + N_1\delta V \\ V_1\delta V + \delta\Phi_T \end{pmatrix}, \tag{50}$$

and $\delta\Phi_T \equiv \hat{G}\delta N_T$ is the perturbed potential due to the tail particles only. The tail potential $\delta\Phi_T$ depends implicitly on the perturbed fluid density δN through Eq. (47), with $\delta\Phi = \hat{G}\delta N$.

This expression for $\hat{C}$ differs from that found in Ref. 1 because here we explicitly separate out the change to the equilibrium density N_1 and velocity V_1 of the pump wave caused by the tail particles, while in Ref. 1 these terms were not separated out, and there $\hat{L}$ was defined in terms of N and V rather than the unperturbed cold fluid equilibrium density and velocity N_0 and V_0. The results using either method are equivalent, and the method used in Ref. 1 is more elegant, but it is useful to explicitly write out all the tail particle dependencies as we do here.

We solve Eq. (49) to first order in the tail density via perturbation theory, writing

$$\psi = A_1\psi_0 + A_2\psi_0^* + \Delta\psi, \tag{51}$$

where A_1 and A_2 are constants to be determined, $\psi_0(s) = (\delta N(s), \delta V(s))$ is the fluid vector eigenmode obtained for no tail particles, satisfying $i\omega_0\psi_0 = \hat{L}\psi_0$, while $\Delta\psi(s)$ is a small correction (of order the tail particle density), chosen to be orthogonal to both ψ_0 and ψ_0^*. We will assume that ω_0 is real and $\delta E_0 = [\psi_0, \psi_0]$ is nonzero (i.e., that we are *not* working with an unperturbed eigenmode for which there is a degeneracy that causes fluid instability).

Now substitute Eq. (51) into Eq. (49), obtaining

$$\begin{aligned} i\omega(A_1\psi_0 + A_2\psi_0^* + \Delta\psi) &= i\omega_0(A_1\psi_0 - A_2\psi_0^*) + \hat{L}\Delta\psi \\ &\quad + A_1\hat{C}\psi_0 + A_2\hat{C}\psi_0^* + \hat{C}\Delta\psi. \end{aligned} \tag{52}$$

The last term $\hat{C}\Delta\psi$ can be dropped because we are working only to first order in the tail density. Now take an inner product of this equation with respect to first ψ_0 and then ψ_0^*, giving two equations. The first equation involves $[\psi_0, \hat{L}\Delta\psi]$ which by Eq. (27) equals $-[\hat{L}\psi_0, \Delta\psi] = -[i\omega_0\psi_0, \Delta\psi] = 0$, since $\Delta\psi$ is orthogonal to ψ_0. Similarly, in the second equation $[\psi_0^*, \hat{L}\Delta\psi] = 0$. We are then left with two equations in the two unknowns A_1 and A_2. In matrix form, these equations are

$$\begin{pmatrix} \omega - \omega_0 + X & Y \\ Y^* & \omega + \omega_0 - X^* \end{pmatrix} \cdot \begin{pmatrix} A_1 \\ A_2 \end{pmatrix} = \begin{pmatrix} 0 \\ 0 \end{pmatrix}, \tag{53}$$

where we have divided through by the factor $i\delta E_0$ and have defined $X \equiv i[\psi_0, \hat{C}\psi_0]/\delta E_0$ and $Y \equiv i[\psi_0^*, \hat{C}\psi_0]/\delta E_0$.

In order for there to be a nontrivial solution to this matrix equation, the determinant of the coefficient matrix must vanish. This implies that the eigenmode frequency ω must satisfy

$$\omega^2 + \omega(X - X^*) + \omega_0(X + X^*) - \omega_0^2 - |X|^2 - |Y|^2 = 0. \tag{54}$$

We will see in a moment that X is real, so the second term in this equation vanishes. Also, we are working only to first order in the tail density, so the X^2 and Y^2 terms can be dropped since they are second order. This implies that, to first order, the eigenmode frequency is given by $\omega^2 = \omega_0^2 - 2X\omega_0$. This implies that instability occurs when $X > \omega_0/2$. Since X is of order the tail density, assumed small, the mode frequency ω_0 must also be small for instability to occur. We are therefore interested in the lowest-frequency fluid modes, as these will be the most easily destabilized by trapped particles. It is therefore useful to define the quantity $\bar{X} = 2X/\omega_0$. In terms of $\bar{X}$, the perturbed wave frequency is given by

$$\omega^2 = \omega_0^2(1 - \bar{X}). \tag{55}$$

Instability occurs when $\bar{X} > 1$.

The inner product required in $\bar{X}$ can be evaluated with the aid of Eqs. (25) and (50),

$$[\psi_0, \hat{C}\psi_0] = \frac{1}{8\pi M}\int ds \begin{pmatrix} \delta\Phi^* + V_0\delta V^* \\ V_0\delta V^* + N_0\delta V^* \end{pmatrix} \cdot \frac{\partial}{\partial s}\begin{pmatrix} N_1\delta V + V_1\delta N \\ V_1\delta V + \delta\Phi_T \end{pmatrix}. \tag{56}$$

This integral can be simplified by integrating by parts and applying Eq. (24), which yields

$$\begin{aligned} \bar{X} &= -\frac{1}{4\pi M\delta E_0}\int ds \begin{pmatrix} \delta V^* \\ \delta N^* \end{pmatrix} \cdot \begin{pmatrix} N_1\delta V + V_1\delta N \\ V_1\delta V + \delta\Phi_T \end{pmatrix} \\ &= -\frac{1}{4\pi M\delta E_0}\int ds\left(N_1|\delta V|^2 + 2V_1 Re(\delta N\delta V^*) + \delta N^*\delta\Phi_T\right). \end{aligned} \tag{57}$$

Compared to Eq. (26), one can see that $\bar{X}$ is simply the negative of the extra fluid energy caused by the trapped particles, compared to half the unperturbed eigenmode energy, $\delta E_0/2$. The factor of two arises because, for stability analysis, we compare the extra trapped particle energy to the mean potential energy of the eigenmode, which is half the total energy for any oscillator. Now that we have derived this, it is not surprising in retrospect that this enters as it does into the frequency shift in Eq. (55), since the square of the frequency of a linear normal mode is proportional to mode energy in any linearized conservative system; see Eq. (34), for example. In fact, we might have skipped the theory leading to this altogether and simply written this expression down directly. Note, by the way, that the signs are such that when $\bar{X}$ is positive, the trapped particle contribution to the eigenmode potential energy is negative, destabilizing the wave by changing the sign of the eigenmode potential energy when $\bar{X} > 1$.

The last term in Eq. (57) can be integrated by parts twice, using Eq. (15) to obtain $\int ds\delta N^*\delta\Phi_T = \int ds\delta\Phi^*\delta N_T$. Then using Eq. (47) to evaluate δN_T we obtain

$$\begin{aligned} \bar{X} &= \frac{1}{2\delta E_0}\int \frac{dsdv}{2\pi M}\frac{\partial f_{T0}}{\partial \epsilon}\left(|\langle\delta\Phi\rangle(\epsilon)|^2 - |\delta\Phi(s)|^2\right) \\ &\quad - \frac{1}{2\delta E_0}\int \frac{ds}{2\pi M}\left(N_1|\delta V|^2 + 2V_1 Re(\delta N\delta V^*)\right). \end{aligned} \tag{58}$$

Here, we have used the following identity: for any function of particle energy $g(\epsilon)$, $\int dsdvg(\epsilon)\delta\Phi^*(s) = \int dsdvg(\epsilon)\langle\delta\Phi\rangle^*(\epsilon)$.

Equation (58) shows explicitly that the energy ratio $\bar{X}$ is a real quantity, so we were justified in setting $X^* = X$ in Eq. (54).

The second line of Eq. (58) did not appear in Eq. (18) of Ref. 1 because there it was subsumed into a contribution to ω_0^2 of first order in the tail density, through the use of N and V rather than N_0 and V_0 in the definition of the operator $\hat{L}$. Here, we explicitly write out all terms proportional to the tail density so that evaluations of their effect on stability are easier to understand.

Equations (55) and (58) are the main theory results that we will use to evaluate parametric instability due to weakly trapped particles. In Sec. IV A, we will evaluate these expressions in various cases and compare results to more intuitive approaches to the theory.

A. Instability of a chain of sharp peaks

We first consider the stability of a pump wave of large amplitude with large $k_\perp$, because we can then make some further analytical progress, and gain some intuition. As discussed in Sec. III, such pump waves resemble a sequence of narrow isolated peaks separated by flat potential sections; i.e., a chain of near-solitons. For simplicity in the following analysis, we define the zero of the potential such that $\Phi_0(\pi) = 0$ in Eq. (29). The low-frequency eigenmodes to the chain of peaks consist of motions of the peaks by small distances $\delta s_n \propto \exp(i\mu s_n)$, $s_n = 2n\pi$, creating perturbations of the form given in Eq. (31).

Substituting these into Eq. (58), we first consider the bounce-average of $\delta\Phi$ that appears in this equation, evaluated via Eq. (48). For particles that are not trapped in the potential wells (i.e., with energy $\epsilon > \epsilon_{max}$ where $\epsilon_{max} = \Phi_0(0)$ is the height of the peaks in potential energy), $\langle\delta\Phi\rangle = 0$ because for each peak in the potential, $\Phi_s'(s)$ in odd in s, but $v(\epsilon, s)$ is even in s. However, for particles trapped between the n – 1st and nth potential peaks (i.e., $2(n-1)\pi < s < 2n\pi$), with $\epsilon < \epsilon_{max}$,

$$\langle\delta\Phi\rangle(\epsilon) = -\frac{2}{\tau(\epsilon)}\int_{s_1}^{s_2}\frac{ds}{v(\epsilon, s)} \times \left(\delta s_{n-1}\Phi_s'(s-2(n-1)\pi) + \delta s_n \Phi_s'(s-2n\pi)\right). \tag{59}$$

Here, s_1 is the left turning point in the potential well created by the two adjacent potential peaks, and s_2 is the right turning point. This can be broken into two integrals, the first integrand peaked near s_1 and the second integrand peaked near s_2. By shifting the origin of coordinates by $2(n-1)\pi$ in each integral, we obtain

$$\langle\delta\Phi\rangle(\epsilon) = -\frac{2\delta s_{n-1}}{\tau(\epsilon)}\int_{\bar{s}_1}^{\bar{s}_2}\frac{ds}{\sqrt{2(\epsilon-\Phi_s(s))}}\Phi_s'(s) - \frac{2\delta s_n}{\tau(\epsilon)}\int_{\bar{s}_1}^{\bar{s}_2}\frac{ds}{\sqrt{2(\epsilon-\Phi_s(s-2\pi))}}\Phi_s'(s-2\pi). \tag{60}$$

where the shifted turning points are locations that satisfy $\epsilon = \Phi_s(\bar{s}_1)$ (on the right side of the peak) and $\epsilon = \Phi_s(\bar{s}_2 - 2\pi)$ (on the left side of the peak). We have also used Eq. (29) with $\Phi_0(\pi) = 0$ to write $v(\epsilon, s) = \sqrt{2(\epsilon - \Phi_s(s))}$ for s near the peak of the first integrand, and $v(\epsilon, s) = \sqrt{2(\epsilon - \Phi_s(s-2\pi))}$ in the second integrand, which is peaked near $s = 2\pi$.

Each integrand can be written as a derivative with respect to s,

$$\langle\delta\Phi\rangle(\epsilon) = \frac{2\delta s_{n-1}}{\tau(\epsilon)}\int_{\bar{s}_1}^{\bar{s}_2} ds\frac{\partial}{\partial s}\sqrt{2(\epsilon-\Phi_s(s))} + \frac{2\delta s_n}{\tau(\epsilon)}\int_{\bar{s}_1}^{\bar{s}_2} ds\frac{\partial}{\partial s}\sqrt{2(\epsilon-\Phi_s(s-2\pi))}, \tag{61}$$

which allows direct evaluation of the integrals, yielding, for trapped particles,

$$\langle\delta\Phi\rangle(\epsilon) = \frac{2\sqrt{2\epsilon}}{\tau(\epsilon)}(\delta s_{n-1} - \delta s_n), \quad \begin{array}{c}\epsilon < \epsilon_{max}\\ 2\pi(n-1) < s < 2\pi n\end{array} \tag{62}$$

where we have used $\Phi_s(\bar{s}_2) = 0$ and $\Phi_s(\bar{s}_1 - 2\pi) = 0$.

Substituting Eqs. (62) and (31) into Eq. (58), and using the non-overlapping nature of the sharply peaked functions in the sums, and the fact that f_{T0} is periodic in s with period 2π, we then obtain

$$\bar{X} = \frac{1}{4\pi M\delta E_0}\sum_{n=1}^{M}\left(|\delta s_{n-1} - \delta s_n|^2\beta - |\delta s_n|^2\int ds\left[N_1(s)V_s'(s)^2 + 2V_1(s)N_s'(s)V_s'(s) + \Phi_s'(s)^2\int dv\frac{\partial f_{T0}}{\partial\epsilon}\right]\right), \tag{63}$$

where β is a phase space integral over the trapped particle distribution given by

$$\beta = \int_{\substack{\epsilon < \epsilon_{max}\\ 0 < s < 2\pi}} ds\,dv\frac{\partial f_{T0}}{\partial\epsilon}\frac{8\epsilon}{\tau^2(\epsilon)}. \tag{64}$$

We will soon see that this expression for β is a more general form of the negative compressibility given by Eq. (5) in the moving wall model.

Equation (63) can be simplified considerably. Consider the integrals in the second and third lines,

$$\int ds\left[N_1(s)V_s'(s)^2 + 2V_1(s)N_s'(s)V_s'(s) + \Phi_s'(s)^2\int dv\frac{\partial f_{T0}}{\partial\epsilon}\right]. \tag{65}$$

First, we note that $(\partial f_{T0}(\epsilon)/\partial\epsilon)\Phi_s'(s)^2 = (\partial f_{T0}(\epsilon)/\partial s)\Phi_s'(s)$, since $\epsilon = v^2/2 + \Phi_s(s)$ wherever $\Phi_s(s)$ is nonzero. The velocity integral of this expression then yields $N_{T0}'(s)\Phi_s'(s)$, where $N_{T0}(s)$ is the equilibrium tail particle density. Since we must integrate this expression over s in Eq. (65), we can integrate by parts twice to obtain

$$\int ds\left[N_1(s)V_s'(s)^2 + 2V_1(s)N_s'(s)V_s'(s) + \Phi_{T0}'(s)N_s'(s)\right], \tag{66}$$

where $\Phi_{T0}(s)$ is the equilibrium potential due to the tail particles. However, according to Eq. (40), $N_s'(s)\Phi_{T0}'(s) = -N_s'(s)(\partial/\partial s)(V_sV_1 + \Phi_1)$, where we replaced V_0 by V_s since we require V_0 only near the peak in N_s'. (We will employ this trick several more times in the following derivation.) Substituting this into Eq. (66) there is a cancelation, and we obtain

$$\int ds\left[N_1V_s'^2 + V_1N_s'V_s' - V_sN_s'V_1' - N_s'\Phi_1'\right]. \tag{67}$$

In the last term, we can integrate by parts twice, replacing $N_s'\Phi_1'$ with $N_1'\Phi_s'$. We can then use $\Phi_s' = -V_sV_s'$ [since Φ_s is an equilibrium fluid potential; see Eq. (38)] to obtain

$$\int ds\left[N_1V_s'^2 + V_1N_s'V_s' - V_sN_s'V_1' + N_1'V_sV_s'\right]. \tag{68}$$

By manipulating the derivatives, the middle two terms in the square bracket can be recast, yielding $V_1N_s'V_s' - V_sN_s'V_1' = (V_1N_s)'(V_s)' - V_1'(N_sV_s)'$. The second term vanishes for an equilibrium flow, see Eq. (37); the first term can be replaced by $-(N_1V_s)'V_s'$, according to Eq. (39). This implies that Eq. (68) becomes

$$\int ds\left[N_1V_s'^2 - (N_1V_s)'V_s' + N_1'V_sV_s'\right]. \tag{69}$$

However, upon expanding the derivatives, this expression vanishes. Therefore, only the first term in Eq. (63) survives, arising from the bounce-average of the perturbed potential

$$\bar{X} = \frac{\beta}{4\pi M\delta E_0}\sum_{n=1}^{M}|\delta s_{n-1} - \delta s_n|^2. \tag{70}$$

This shows that the energy ratio $\bar{X}$ is nonzero only when there is a distribution of trapped particles, since $\beta = 0$ otherwise. Using Eqs. (32)–(34) and performing the sum, Eq. (70) simplifies to

$$\bar{X} = \frac{\beta}{\mathscr{K}}. \tag{71}$$

Thus, in the chain of sharp peaks model the energy ratio $\bar{X}$ is the ratio of the negative compressibility β to the spring constant $\mathscr{K}$. The instability criterion $\bar{X} > 1$ is equivalent to $\beta > \mathscr{K}$: the negative compressibility is large enough to overcome repulsion between the density peaks, changing the sign of the potential energy.

Applying Eqs. (71) and (33) to Eq. (55) yields the perturbed mode frequency

$$\omega^2 = 4\frac{\mathscr{K} - \beta}{\mathscr{M}} \sin^2(\pi\mu). \tag{72}$$

This dispersion relation recovers Eq. (9), but for a more general wave potential structure and for a general trapped particle distribution.

For very narrow peaks, we can treat the peaks as moving walls as was done in deriving Eq. (9), and then the negative compressibility β given by Eq. (64) can be further simplified by noting that trapped particles in effect perform specular reflections off of the walls, with period $\tau(\epsilon) = 4\pi/v$ where $v(\epsilon) = \sqrt{2\epsilon}$ is the speed of particles moving between the walls. When this approximation is used in Eq. (64), and an integration by parts is performed, the result can be expressed as

$$\beta = \frac{6}{2\pi}\int_0^{v_{max}} dv v^2 \left(f_{T0}(v_{max}) - f_{T0}(v)\right). \tag{73}$$

and where $v_{max} = \sqrt{2\epsilon_{max}}$ is the speed of particles at the separatrix between trapped and passing particles, and here, we consider the distributions to be functions of velocity rather than energy. This expression for β recovers the moving wall approximation Eq. (5).

V. PARTICLE IN CELL (PIC) SIMULATIONS COMPARED TO THEORY

In this section, we describe particle in cell simulations of the trapped-particle parametric instability, and comparison of the observed instability growth rates to the theory. Simulations were performed in the pump wave frame with periodic boundary conditions of period 4π, i.e., twice the pump wavelength. This period allows eigenmodes with $\mu = 0$ or $\mu = 1/2$. The total number $\mathbb{N}_{sim}$ of particles in these simulations was 10^6. The particles were stepped forward in time using the second-order leapfrog method with a time step $\Delta t = 0.04$. The potential was evaluated using a fast Fourier transform solution of the Poisson equation on a 600 element uniform grid, with density determined using standard linear interpolation to the grid. Most of the particles were given initial velocities $v = V_0(s)$ and were randomly distributed in s with density $N_0(s)$ in such a way as to self-consistently form a pump wave with wave potential $\Phi_0(s)$. These particles constituted the cold fluid, all with equal particle energy $\epsilon_0 \equiv V_0^2/2 + \Phi_0$.

A relatively small number $\mathbb{N}_T$ of added particles formed the tail distribution, making up the remainder of the 10^6 particles in the simulation. We chose this distribution to be uniform in phase space between some energy ϵ_{min} and the fluid energy ϵ_0, and zero otherwise. Particles were therefore placed randomly within this phase space region, with uniform weighting. An example of the resulting initial velocity distribution is displayed in Fig. 6, and particle energies are displayed in Fig. 7, compared to the fluid potential energy $\Phi_0(s)$. Only a small fraction of the tail particles are trapped in the wave potential, and one might think that the simulation could be run more efficiently by adding only trapped particles in the tail, neglecting the untrapped tail particles. However, it is well known that energy distributions with gaps between filled energy surfaces are beam-unstable.[17] These instabilities are avoided for our uniform distribution, or for others with monotonically increasing dependence on energy in the wave frame up to the fluid energy ϵ_0. Such beam-stable BGK distributions are quite commonly produced through excitation of large amplitude waves on a collisionless plasma.[18–21]

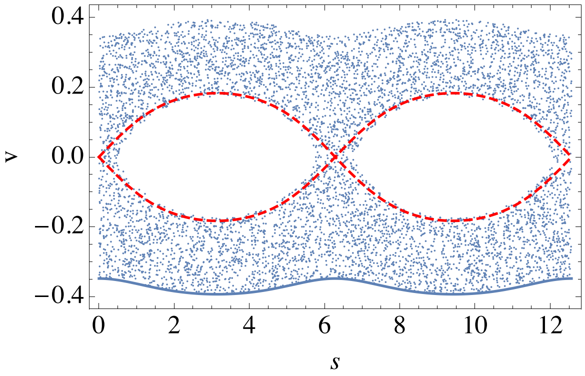

FIG. 6. Initial distribution of particles in a PIC simulation for which $k_\perp = 2.5$, $A = 0.03$. 993 000 particles have equal energies ϵ_0 forming a self-consistent pump wave [the solid curve at the bottom of the figure, consisting of particles for which $v = V_0(s)$]. $\mathbb{N}_T = 7000$ tail particles are distributed uniformly in phase space between $\epsilon_{min} = 0.9\epsilon_{max}$ and ϵ_0. 427 of these particles are trapped, with energies less than the separatrix energy ϵ_{max}. Separatrices are shown by the dashed curves.

Simulations were carried out for two values of $k_\perp$, $k_\perp = 2.5$ and $k_\perp = 5$, for various amplitudes A. In the first set of simulations, ϵ_{min} was chosen to be $\epsilon_{min} = 0.9\epsilon_{max}$, so that a given fraction of the tail particles were trapped in the pump wave potential. Holding these parameters fixed, the number of tail particles $\mathbb{N}_T$ was then varied from 0 up to 20 000. An instability was then observed to develop, growing out of noise, with a growth rate depending on $\mathbb{N}_T$. The instability growth rate was measured two ways: By evaluating the time-dependent change in fractional displacement $\lambda(t) = (\delta s_2(t) - \delta s_1(t))/(2\pi)$ between two adjacent peaks in the simulated wave potential; and by evaluating a moment of the particle density which has a strong overlap with the growing eigenmode. We chose the moment $m_j(t) = |\int_0^{4\pi} dsn(s,t)\exp(ijs/2)|$, taking $j = 1$, where $n(s, t)$ is the total particle density observed in the simulation. A typical case is shown in Figs. 8 and 9. An exponential fit to the growth was then made in order to obtain the growth rate. The growth rates determined with these two methods typically agreed to 10% or better.

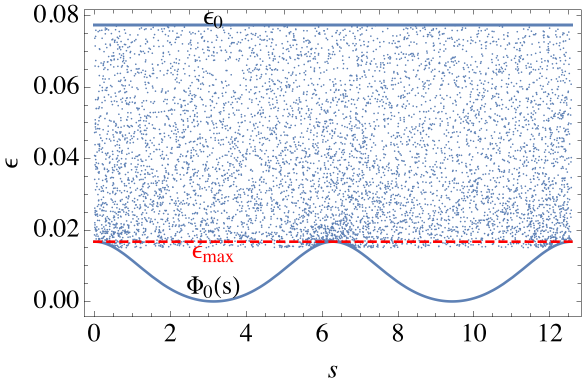

FIG. 7. Same as in Fig. 6 but energies are plotted rather than velocities.

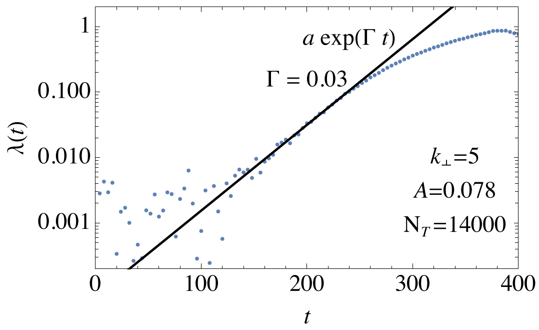

FIG. 8. Fractional change in distance between adjacent potential peaks vs time, with a fit to an exponential.

After the exponential growth phase, a complex nonlinear bouncing of the density moments occurs, as shown in Fig. 9. This is an irreversible process, as trapped particles in the waves respond to the large amplitude motions by beginning to fill in the phase-space holes in the distribution function. This irreversible nonlinear process heats the plasma. An animation of the instability is included with the online materials, which clearly shows how trapped particles are passed from one potential well to the other as the instability grows. Figure 10 (Multimedia view) is an image taken from this animation, showing the phase-space in the nonlinear phase of the instability. Particles that were initially trapped in the compressing well (green) have been forced into the expanding well and have been cooled, leaving a beam-unstable gap in the particle distribution function that will eventually fill in as untrapped particles (blue) are drawn into the gap due to the beam instability. Narrow cats eyes due to Landau resonances can also be observed, causing more irreversibility.

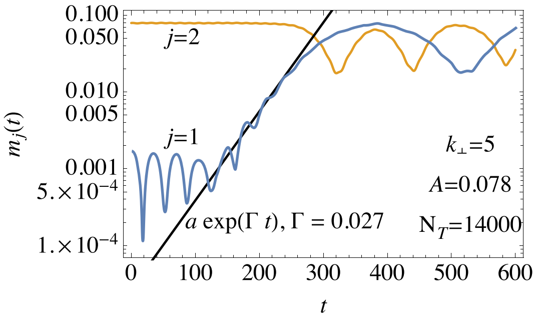

FIG. 9. Two density moments, plotted over a longer time than in Fig. 8, and a fit to an exponential for the growing $j=1$ moment. The $j=2$ moment has a strong overlap with the initial pump wave.

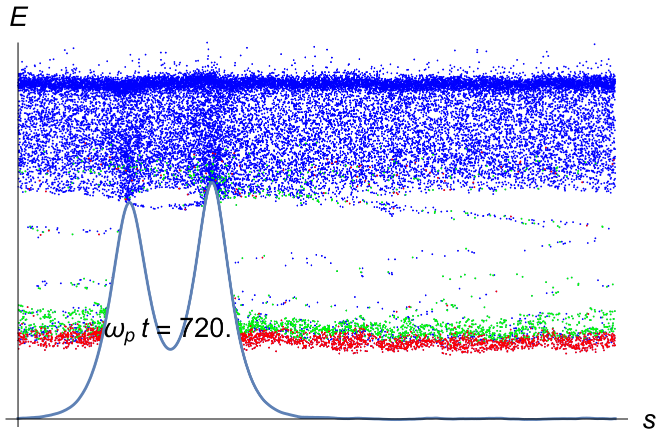

FIG. 10. The nonlinear phase of the instability for $A = 0.078$, $k_\perp = 5$, $\epsilon_{min} = 0.9\epsilon_{max}$. Particle energies and positions are plotted as well as the potential. Green particles were initially trapped in the compressed well, but were detrapped and retrapped in the expanding well, where they lay atop the trapped particles initialized in that well (red). This is a higher resoluion simulation than the others in the paper, run with 10^7 particles and $\mathbb{N}_T = 20\,000$ (equivalent to the $\mathbb{N}_T = 2000$, $\mathbb{N}_{sim} = 10^6$ point in Fig. 12). Multimedia view: https://doi.org/10.1063/1.5116376.1

Figures 11 and 12 display the growth rates determined in the linear phase of the instability, plotted as the number of tail particles is varied, fixing the other parameters to the values shown. We compare these simulation results to the theory predictions for the low-frequency $\mu = 1/2$ eigenmode discussed previously, for which adjacent peaks move in opposite directions. The solid lines in the figure are the predictions of Eq. (55) with the energy ratio $\bar{X}$ evaluated from Eq. (58). For each theory curve, corresponding to given values of $k_\perp$ and A, the equilibrium functions N_0, V_0, Φ_0 are evaluated from solutions to Eqs. (16)–(18). Corrections N_1 and V_1 to the equilibrium, caused by the tail distribution, are then determined by solving Eqs. (39)–(42), evaluated for the unit tail particle number. Since the equations are linear in the tail density, the results can be multiplied by $\mathbb{N}_T$. The cold fluid $\mu = 1/2$ low-frequency eigenmode is then evaluated via Hills method, providing $\delta N(s), \delta V(s), \delta\Phi(s), \omega_0$ and δE_0. From Eq. (58), the required phase space integral over the uniform tail distribution can be carried out analytically, yielding

$$\bar{X} = \frac{1}{2\delta E_0}\frac{\tau(\epsilon)}{4\pi} f_{T0}\, 2\Big(|\langle\delta\Phi\rangle(\epsilon)|^2 - \langle|\delta\Phi|^2\rangle(\epsilon)\Big)\Big|_{\epsilon=\epsilon_0}^{\epsilon=\epsilon_{min}} - \frac{1}{2\delta E_0}\int_0^{4\pi}\frac{ds}{4\pi}\big(N_1|\delta V|^2 + 2V_1 Re(\delta N \delta V^*)\big). \tag{74}$$

The bounce period $\tau(\epsilon)$ and the bounce averages are each evaluated at the required energies ϵ_{min} and ϵ_0 (noting that for untrapped particles

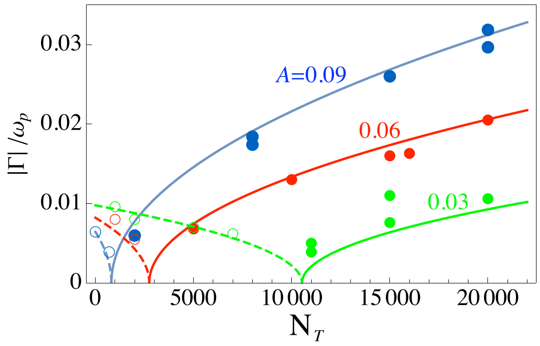

FIG. 11. Growth rates and oscillation frequencies for the trapped-particle parametric instability vs the number $\mathbb{N}_T$ of tail particles for the tail distribution discussed in the text with $\epsilon_{min} = 0.9\epsilon_{max}$, for $k_\perp = 2.5$ and for three amplitudes: $A = 0.03$, $0.06, 0.09$. Solid dots are instability growth rates determined from PIC simulations. Open circles are stable oscillation frequencies. Curves are the theory predictions for the three amplitudes, from Eqs. (55) and (74).

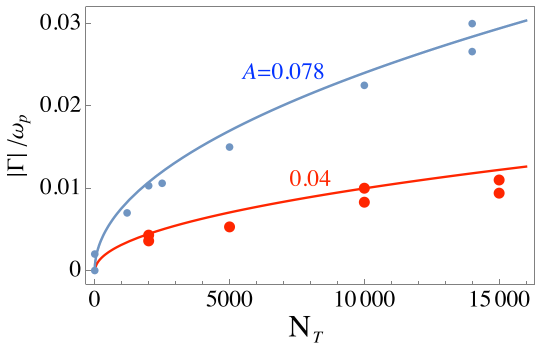

FIG. 12. Same as for Fig. 11, but for $k_\perp = 5$ and for two amplitudes: $A = 0.04, 0.078$. Solid dots are instability growth rates determined from PIC simulations. Curves are the theory predictions for the two amplitudes, from Eqs. (55) and (74).

at $\epsilon = \epsilon_0$, $\langle\delta\Phi\rangle = 0$). Note that the energy ratio $\bar{X}$ is proportional to tail particle number $\mathbb{N}_T$ through its dependence on f_{T0} in the first line of the equation and its dependence on N_1 and V_1 in the second line. In particular, the constant $f_{T0} = 4\pi\mathbb{N}_T/(\mathbb{N}_{sim}\mathscr{A})$ where $\mathscr{A}$ is the phase-space area between the energy surfaces ϵ_0 and ϵ_{min} in the computation region $0 < s < 4\pi$. The factor of $4\pi/\mathbb{N}_{sim}$ arises because

$$\frac{\mathbb{N}_T}{\mathbb{N}_{sim}} = \frac{\int_0^{4\pi} ds \int_{\epsilon_{min}<\epsilon<\epsilon_0} f_{T0}\, dv}{\int_0^{4\pi} ds N} = \frac{f_{T0}\mathscr{A}}{4\pi}, \tag{75}$$

where the denominator equals 4π because the mean value of the density is unity in our units.

The theory curves evaluated in this manner are in fairly close agreement with the simulations for all cases; although at low wave amplitudes the growth rates became more difficult to measure in the simulations and there was more scatter in repeated measurements. For the $k_\perp = 2.5$ cases, at low tail particle numbers $\bar{X}$ was less than one, insufficiently large to cause instability. The theory gives an imaginary value of Γ in this regime (dashed curves in Fig. 11). Open circles in the plot correspond to simulation results for which there was no observed instability; rather, peaks in the pump wave oscillated around their equilibrium locations. This caused the observed quantities $\lambda(t)$ and $m(t)$ to oscillate at the frequencies plotted in the figure. However, for sufficiently large numbers of weakly trapped particles even the lowest-amplitude wave with $A = 0.03$ was driven unstable (11 000 tail particles was sufficient, which is only about 700 trapped particles out of the total of 10^6). For the $k_\perp = 5, A = 0.078$ case, the mode frequency ω_0 is small enough so that only one thousand tail particles (corresponding to only 220 trapped particles) were sufficient to provoke a measurable instability. Here, the instability growth rate is proportional to the square root of the number of trapped particles.

This theory is also compared to the simpler versions of the theory, in Table I. It is interesting to note that in the exact calculation of Eq. (74), $\bar{X}$ is dominated by the term in the equation proportional to $|\langle\delta\Phi\rangle(\epsilon)|^2$ in all but the lowest-amplitude wave given by the first line in the table; the other terms in the equation cancel with one-another nearly exactly, as expected in the simpler theories. For the simpler theories, the energy ratio $\bar{X}$ is evaluated using Eq. (71) with the negative compressibility coefficient β evaluated in both the Eq. (64) "chain of sharp peaks" approximation and the more extreme moving wall approximation, Eq. (5). Under the first "chain of peaks" approximation, Eqs. (71), (64), and (75) imply that, for our uniform tail phase-space density,

$$\bar{X} = \frac{32\pi\epsilon_{min}}{\tau(\epsilon_{min})\mathscr{K}\mathscr{A}} \frac{\mathbb{N}_T}{\mathbb{N}_{sim}}. \tag{76}$$

For the moving wall approximation, taking $\epsilon_{min} = v_{min}^2/2$ and $\tau(\epsilon_{min}) = 4\pi/v_{min}$ in Eq. (76),

$$\bar{X} = \frac{4v_{min}^3}{\mathscr{K}\mathscr{A}} \frac{\mathbb{N}_T}{\mathbb{N}_{sim}}. \tag{77}$$

In keeping with the moving wall approximation of very narrow potential peaks separated by regions with zero potential, we further simplify here by taking $\mathscr{A} = 8\pi(v_0 - v_{min})$ in Eq. (75), where $v_0 = \sqrt{2\epsilon_0}$.

For $k_\perp = 5$ and $A = 0.078$, Table I shows that the "sharp peaks approximation," Eq. (76), is within 15% of the full numerical calculation for $\bar{X}$ given by Eq. (74), while the moving wall approximation, Eq. (77), is within 40%. For lower amplitude A and lower $k_\perp$ the three theories have the same general trends, but the approximate values for $\bar{X}$ fare less well compared to the exact result, as one would expect given the approximations involved. The smallest amplitude and smallest $k_\perp = 2.5$ case is not well-described by a chain of isolated peaks since the pump wave is nearly a single Fourier mode at this low amplitude [see the fluid velocity $V_0(s)$ displayed in Fig. 6 and the fluid potential $\Phi_0(s)$ displayed in Fig. 7]. For this case, the fits used to obtain $\mathscr{M}$, based on Eqs. (31) and (34), are poor.

A second set of simulations was also carried out, taking $\epsilon_{min} = 1.2\epsilon_{max}$. In this case, there are no trapped particles in the pump wave potential. In these simulations, no instability was observed, for the values of $A, k_\perp$ and $\mathbb{N}_T$ that resulted in instability in the previous

TABLE I. Parameters used in the PIC simulations, and corresponding theory predictions for the energy ratio $\bar{X}$, for $\epsilon_{min} = 0.9\epsilon_{max}$. Instability requires $\bar{X} > 1$.

$k_\perp$	A	Fluid energy ϵ_0	Separatrix energy ϵ_{max}	Fluid freq: $\omega_0(\mu = 1/2)$	Peak mass $\mathscr{M}$	Exact theory $\bar{X}\mathbb{N}_{sim}/\mathbb{N}_T$ Eq. (74)	Sharp peaks approximation $\bar{X}\mathbb{N}_{sim}/\mathbb{N}_T$ Eq. (76)	Moving wall approximation $\bar{X}\mathbb{N}_{sim}/\mathbb{N}_T$ Eq. (77)
2.5	0.03	0.0774	0.0167	9.764×10^{-3}	0.8	95	400	200
2.5	0.06	0.0866	0.0346	8.203×10^{-3}	1.4	365	670	630
2.5	0.09	0.0974	0.0546	6.427×10^{-3}	1.747	1230	1630	2110
5	0.04	0.0228	0.00742	3.676×10^{-4}	0.668	7.38×10^4	1.76×10^5	1.11×10^5
5	0.078	0.0300	0.0206	3.916×10^{-5}	1.073	3.71×10^7	4.26×10^7	5.17×10^7

simulations. We take this as more strong evidence that the observed instability is caused by trapped particles.

A third set of simulations took $\epsilon_{min} = 0$. In this case, the pump wave potential wells are uniformly filled with trapped particles. In almost all cases, no instability was observed in these simulations as well, as expected from Eq. (76). This indicates that it is not enough to have trapped particles; for this instability, the particles must be weakly trapped, with more trapped particles near the separatrix energy ϵ_{max} and fewer in the bottom of the potential wells.

However, in one case, $A = 0.078, k_\perp = 5$, something like a weak instability occurred. For this large amplitude and large $k_\perp$ case, the theory predicts a (nearly) neutrally stable situation: Without trapped particles, the oscillation frequency of the peaks is quite small (see Table I); and $\bar{X}$ vanishes [see, for example, Eq. (76)]. The fractional displacement $\lambda(t)$ between adjacent peaks in the simulation is plotted in Fig. 13. Initially, the distance $\lambda(t)$ increases slowly with time, which one might expect: In a finite particle simulation, the potential fluctuates slightly in time. if one peak happens to fluctuate to a slightly higher value than the other, it will pickup speed (soliton speed depends on the potential height) and eventually catch up to the next peak. This is not unexpected, and is not an instability; it is merely a slow large amplitude (but low energy) fluctuation of a (nearly) neutrally stable mode, and is observed in the simulations even in the absence of trapped particles. However, the peaks appear to accelerate as they approach one-another more closely. This acceleration is likely a nonlinear trapped particle effect, since it is not predicted in linear theory and does not occur without trapped particles. However, an explanation will likely require a nonlinear theory of trapped particle effects and so will be pursued in future work. In any case, the instability develops on a much longer time scale than occurs for the same pump wave parameters but with a weakly trapped distribution [Fig. 8].

VI. r-z PIC SIMULATIONS COMPARED TO EXPERIMENT

Experiments have observed parametric instability of large amplitude TG waves in a cylindrical non-neutral plasma column.[2,22] However, the plasma column was of finite length L_p and consequently, the pump waves were not traveling waves, but were instead nonlinear standing waves. For low amplitudes, density perturbations in such a wave are sinusoidal

$$\delta n(r, z, t)/n_0 = A(t) J_0(k_\perp r) \cos(\omega_2 t) \cos(k_2 z), \tag{78}$$

where $k_n \approx n\pi/L_p$ is the parallel wavenumber of a standing wave with mode number n, ω_2 is the pump wave frequency, $A(t)$ is the wave amplitude, and J_0 is a Bessel function.

The standing wave was created by driving a sinusoidal voltage on one of the confinement electrodes for several cycles at the $n = 2$ mode frequency ω_2. This frequency was determined experimentally, but is close to the cold-fluid prediction $\omega_n = \omega_p k_n / \sqrt{k_\perp^2 + k_n^2}$ with $k_\perp = \sqrt{2/\ln(r_e/r_p)}/r_p$, where r_e is the electrode radius and r_p is the plasma radius. The resulting wave was detected by measuring image charge fluctuations on a second confinement electrode. Details can be found in Refs. 2 and 23. If the amplitude A was large enough a growing daughter wave with wavenumber $k_1 = k_2/2$ and frequency $\omega_1 \approx \omega_2/2$ was observed. Four sets of experimental data are displayed in Fig. 14 for four different plasma temperatures. Growth rates for the instability are plotted vs the amplitude A. As one expects in a parametric instability, the growth rate depends on pump wave amplitude, but it also depends on plasma temperature. Hotter plasmas are more easily driven unstable. We believe that this is because hotter plasmas produce more trapped particles in a wave of a given amplitude. However, the trapped particles are too few in number to be experimentally observable, even with LIF diagnostics available on the experiment that were used to measure the velocity distribution function. Furthermore, the theory in Secs. II–IV is applicable to traveling waves, but not directly applicable to standing waves.

Therefore, in order to test the theory that the instability is caused by trapped particles, we have carried out PIC simulations of these experiments in cylindrical geometry with realistic plasma confinement potentials. These simulations employed a similar driving potential to that used to excite the pump wave in the experiments, on plasmas with similar temperatures and densities to those used in the experiments. Similar simulations have been compared to the experiments previously,[2,23] but the simulations performed for this paper are for a finite length plasma confined in z by realistic end potentials, as opposed to the infinite plasma cylinder with periodic boundary

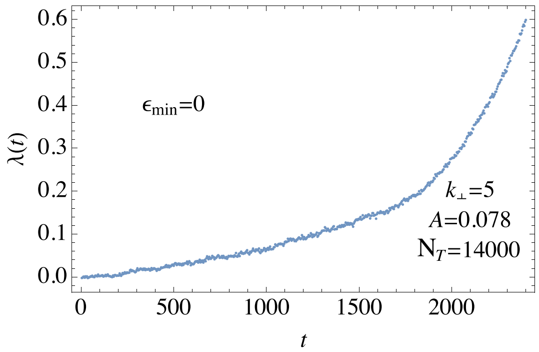

FIG. 13. Fractional change in the displacement between adjacent peaks vs time, for a tail distribution that completely and uniformly fills the potential wells. Note the longer time scale compared to Fig. 8, which is for the same parameters but with $\epsilon_{min} = 0.9\epsilon_{max}$.

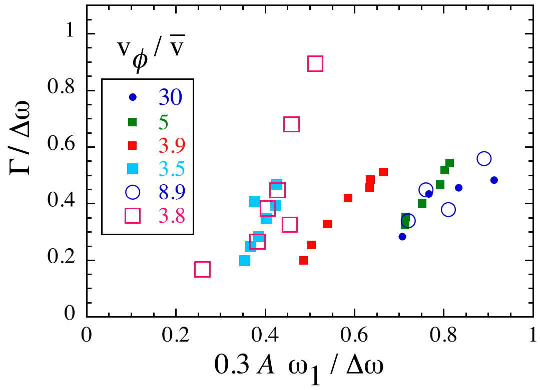

FIG. 14. Parametric instability growth rate in experiments, and in r–z PIC simulations. Dots are experimental measurements vs pump amplitude A, for four different plasma temperatures parameterized by the ratio of the wave phase velocity to the thermal speed, $v_\phi/\bar{v}$. Open symbols are results from PIC simulations at two different temperatures. Here, $\Delta\omega = 2\omega_1 - \omega_2$.

conditions used previously. The PIC simulations used here solved for the dynamics of charges moving only in the z direction, on a grid of radii. A typical run used 10^6 particles moving through a computational grid of 60 radial grid points out to the electrode radius $r_e = 2.86$ cm, and 320 grid points in the z direction over the computational length of $L_c = 23.3$ cm. Distances in the simulation were measured in units of L_c and times were in units of the plasma frequency at a density of 10^6 cm^{-3}. Timesteps in these units were taken as $\Delta t = 0.06$, using the leapfrog method. Densities at each radial gridpoint were referred to the z grid using standard linear interpolation. The cylindrical geometry Poisson equation was then solved on the r – z grid using the SLATEC banded matrix solver SNBFS. As in the experiments, the plasma radius was roughly 0.5 cm, the plasma length was roughly 14 cm, and the central density was roughly 2×10^7 cm^{-3}. Results from two sets of simulations are displayed, for two different plasma temperatures. The coldest achievable temperature in the simulation was 0.1 eV, producing a pump wave with a phase velocity $v_\phi = \omega_2/k_2$ compared to thermal speed $\bar{v} = \sqrt{T/m}$ of roughly $v_\phi/\bar{v} \approx 8.9$.

For a low amplitude wave, there would be essentially no trapped particles for such a low temperature plasma; but at large amplitudes the wave potential is large enough to accelerate particles out of the edges of the velocity distribution function, trapping them in the wave. A snapshot of the particle locations in $z - v_z$ phase space at $r = 0$ is shown in Fig. 15 (Mulitmedia view), for the simulation point farthest to the right in Fig. 14. The snapshot is taken at time $t = 400$, after the excitation of the pump wave to an amplitude $A = 0.35$, but before the daughter wave has had a chance to grow up from noise. Two large hollow "cats eyes" consisting of weakly trapped particles can be observed wrapping around the plasma periphery. The cats eyes are distorted, narrowing as they fold around the plasma ends, and the x-points in the cats eyes are substantially smeared, presumably by chaotic particle orbits. An animation of the wave excitation and particle trapping is available in the electronic materials accompanying the paper; it shows that particles in the plasma ends are pulled out of the distribution as the cats eyes travel clockwise around the periphery of the plasma in phase space (the wave phase speed is $v_\phi \approx 0.1$ in the units of the simulation).

Parametric instability was observed in these simulations. The instability was measured in a variety of ways, but in Fig. 16 we display the results of a measurement method that is also used in the experiments: We fit the image charge $\sigma(t)$ picked up on an electrode at the wall radius to the functional form $\sigma(t) = \sigma_0 + a_1 \sin(\omega_1 t + \phi_1) + a_2 \sin(\omega_2 t + \phi_2)$, where the fit is performed in an overlapping sequence of short time ranges of length $\delta t = 20$, which is roughly three oscillation periods of the pump wave. The fit parameters a_1 and a_2 are displayed for each element of the sequence vs the center time at which the fit is taken (i.e., the starting time of the fit plus $\delta t/2$). After the drive was turned off, the amplitude a_1 of the daughter wave grew exponentially to about 20 times its original amplitude, and then displayed more complex nonlinear behavior not unlike that seen in the 1D simulations. In the animation accompanying Fig. 15, the growth of the $n = 1$ daughter wave can be most easily observed by focussing on the shape of the outer envelope of the cats-eye at late times; this envelope becomes asymmetrical as particles slosh from end to end in the growing $n = 1$ mode, and the cats eyes fill in.

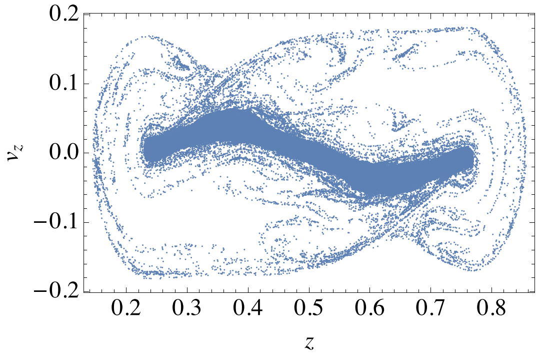

FIG. 15. Snapshot of particle z positions and z velocities at the $r = 0$ radial grid point in a PIC simulation of a large amplitude TG standing wave. Multimedia view: https://doi.org/10.1063/1.5116376.2

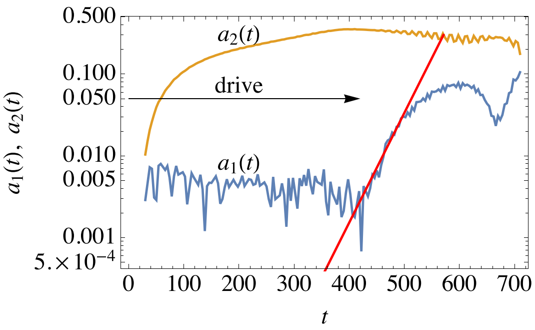

FIG. 16. Amplitudes of the pump wave and the daughter wave, a_2 and a_1 respectively, measured from wall signals in the simulation, for the plasma mode whose distribution is shown in Fig. 15. Also shown is the time over which the pump wave is driven, and an exponential fit to the amplitude of the daughter wave.

The open symbols in Fig. 14 show the growth rates vs pump amplitude observed in the simulations of the cold plasma, and also of a warmer plasma with $v_\phi/\bar{v} = 3.8$. As expected, there are substantially more trapped particles in the warmer plasma, for a given pump wave amplitude. We observed higher growth rates in the warm plasma runs for a given pump wave amplitude, and a longer period of exponential growth, with the daughter waves growing by a factor of roughly 100 before nonlinear oscillations occurred. This is consistent with the theory that instability is driven by trapped particles. The growth rates measured in the simulations show quite similar dependence on pump wave amplitude and on temperature compared to the experiments.

As a final test of the trapped particle mechanism, we artificially removed trapped particles from the simulations at every time step (identifying trapped particles as any particles with speed $|v_z|$ greater than the phase velocity $v_\phi = 0.1$), resetting their speeds below the range necessary for trapping. We found that this turned off the unstable growth of the daughter wave (see Fig. 17).

VII. DISCUSSION

In this paper, we have seen that nonlinear waves can be destabilized via collisionless adiabatic detrapping and retrapping of particles that are weakly trapped in wave potential wells. Energy drawn from the trapped particle distribution through this adiabatic mechanism drives a parametric instability, with a maximum growth rate when the daughter waves have twice the pump wavelength. For large amplitude

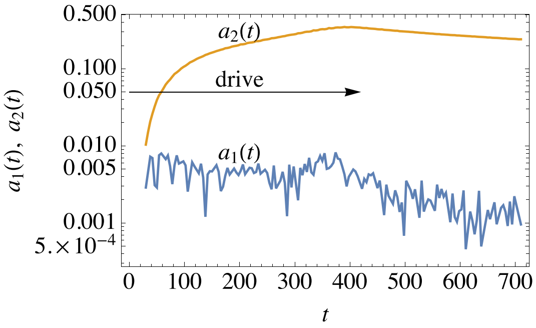

FIG. 17. Same drive and initial condition as in Fig. 16, but with trapped particles removed as described in the text.

waves, the growth rate is roughly proportional to the square root of the fraction of trapped particles, but the trapped particle distribution must be weakly trapped, with more trapped particles near the pump wave separatrices than in the bottom of the potential wells.

The theory presented here applies to nonlinear traveling waves, but current experiments excite standing waves in plasma columns of finite length. While simulations presented here show that trapped particles are implicated in the parametric instability observed in experiments, the theory needs to be generalized to account for standing waves. However, it might be possible in certain experimental geometries[24] to directly test the theory for traveling TG waves.

Detrapping and retrapping of weakly trapped particles have previously been connected to several important transport processes in weakly collisional plasmas,[16,25,26] such as super-banana transport.[27,28] Collisional scattering of trapped particles across a separatrix has also been predicted to either stabilize or destabilize linear trapped particle modes.[29,30] In this paper, the destabilizing mechanism is collisionless and adiabatic, and is therefore reversible in the linear regime. However, in the nonlinear regime irreversible processes set in through the onset of secondary beam instabilities and through Landau resonances and chaos at the wave separatrices, effects that are not included in the linear analysis presented here but which can be observed in the simulations. These irreversible processes eventually cause phase space holes in the weakly trapped distribution to fill in, which may be an important nonlinear wave heating mechanism. This may be of some importance in the context of Alfvén waves in the solar corona. The instability mechanism may also be active in other waves with near-acoustic dispersion relations, such as in the parametric instabilities observed in electron acoustic waves.[31] These questions will be investigated in future work.

ACKNOWLEDGMENTS

The author acknowledges useful discussions with Professor T. M. O'Neil, Professor C. F. Driscoll, and Dr. Matt Affolter. Dr. Affolter also provided the author with the experimental data in Fig. 14 (previously published in Ref. 2). This work was supported by U.S. DOE Grant No. DE-SC0018236 and NSF Grant No. PHY-1805764.

REFERENCES

[1] D. H. E. Dubin, Phys. Rev. Lett. **121**, 015001 (2018).
[2] M. Affolter, F. Anderegg, D. H. E. Dubin, F. Valentini, and C. F. Driscoll, Phys. Rev. Lett. **121**, 235004 (2018).
[3] R. C. Davidson, *Methods in Nonlinear Plasma Theory* (Academic Press, NY, 1972), Sect. 14.5.
[4] C. B. Wharton, J. H. Malmberg, and T. M. O'Neil, Phys. Fluids **11**, 1761 (1968).
[5] W. L. Kruer, J. M. Dawson, and R. N. Sudan, Phys. Rev. Lett. **23**, 838 (1969).
[6] D. H. E. Dubin and A. Ashourvan, Phys. Plasmas **22**, 102102 (2015).
[7] D. H. E. Dubin, Phys. Plasmas **26**, 102111 (2019).
[8] I. Y. Dodin, P. F. Schmit, J. Rocks, and N. J. Fisch, Phys. Rev. Lett. **110**, 215006 (2013).
[9] P. F. Schmidt, I. Y. Dodin, J. Rocks, and N. J. Fisch, Phys. Rev. Lett. **110**, 055001 (2013).
[10] A. W. Trivelpiece and R. W. Gould, J. Appl. Phys. **30**, 1784 (1959).
[11] J. H. Malmberg and C. B. Wharton, Phys. Rev. Lett. **17**, 175 (1966).
[12] W. M. Mannheimer, Phys. Fluids **12**, 2426 (1969).
[13] B. Deconinck and J. N. Kutz, "Computing spectra of linear operators using the Floquet-Fourier-Hill method," J. Comput. Phys. **219**, 296 (2006).
[14] C. Kittel, *Introduction to Solid State Physics*, 5th. ed. (John Wiley and Sons, New York, 1976), p. 108.
[15] I. B. Bernstein, J. M. Greene, and M. D. Kruskal, Phys. Rev. **108**, 546 (1957).
[16] D. H. E. Dubin, Phys. Plasmas **24**, 112120 (2017).
[17] T. M. O'Neil and J. H. Malmberg, Phys. Fluids **11**, 1754 (1968).
[18] W. L. Kruer and J. M. Dawson, Phys. Fluids **13**, 2747 (1970).
[19] F. Valentini, T. M. O'Neil, and D. H. E. Dubin, Phys. Plasmas **13**, 052303 (2006).
[20] L. Demeio and J. P. Dorning, J. Plasma Phys. **46**, 63 (1991).
[21] J. R. Danielson, F. Anderegg, and C. F. Driscoll, Phys. Rev. Lett. **92**, 245003 (2004).
[22] H. Higaki, Plasma Phys. Controlled Fusion **39**, 1793 (1997).
[23] M. Affolter, F. Anderegg, D. H. E. Dubin, F. Valentini, and C. F. Driscoll, "Fluid and kinetic nonlinearities of near-acoustic plasma waves," Phys. Plasmas (submitted).
[24] M. R. Stoneking, J. P. Marler, B. N. Ha, and J. Smoniewski, Phys. Plasmas **16**, 055708 (2009).
[25] D. H. E. Dubin, C. F. Driscoll, and Yu. A. Tsidulko, Phys. Rev. Lett. **105**, 185003 (2010).
[26] D. H. E. Dubin, A. A. Kabantsev, and C. F. Driscoll, Phys. Plasmas **19**, 056102 (2012).
[27] H. Mynick, Phys. Plasmas **13**, 058102 (2006).
[28] A. A. Galeev, R. Z. Sagdeev, H. P. Furth, and M. N. Rosenbluth, Phys. Rev. Lett. **22**, 511 (1969).
[29] M. N. Rosenbluth, D. W. Ross, and D. P. Kostamorov, Nucl. Fusion **12**, 3 (1972).
[30] A. A. Kabantsev, C. F. Driscoll, T. J. Hilsabeck, T. M. O'Neil, and J. H. Yu, Phys. Rev. Lett. **87**, 225002 (2001).
[31] A. A. Kabantsev, F. Valentini, and C. F. Driscoll, "Experimental investigation of electron-acoustic waves in electron plasmas," AIP Conf. Proc. **862**, 13–18 (2006).